

# Experimental and Numerical Researches on the Seismic Behavior of Tubular Reinforced Concrete Columns of Air-Cooling Structures

Ning-jun Du, Guo-liang Bai, Ya-zhou Xu\*, and Chao-gang Qin

(Received February 20, 2016, Accepted June 16, 2017, Published online September 13, 2017)

**Abstract:** Tubular reinforced concrete columns of air-cooling condenser structures, which undertake the most weight of air cooling equipment, are the major components to resist lateral forces under earthquake. Once collapsed, huge casualties and economic loss would be caused. Thus, four 1/8 scaled specimens were fabricated and tested through the pseudo-static testing method. Failure modes and crack patterns of the specimens under cyclic loading were observed. Then, finite element models of tubular reinforced concrete columns were established using OpenSees and were verified with the experimental results. Finally, the influence of axial compression ratio and longitudinal reinforcement on energy dissipation capacity and stiffness degradation were studied based on the validated finite element modes. It is confirmed that tubular reinforced concrete columns of air-cooling condenser structure exhibit a moderate ability of energy dissipation, and the nonlinear finite element model could reasonably simulate its seismic behavior. Furthermore, axial compression ratio and longitudinal reinforcement are main factors which affect the seismic behavior of the tubular reinforced concrete columns. The experimental results and simulation method provide an available way to design this kind of large tubular reinforced concrete columns with thin-wall.

**Keywords:** tubular reinforced concrete column, seismic performance, pseudo-static test, OpenSees.

## 1. Introduction

Compared with the traditional natural draft cooling process, the direct air-cooling technique can achieve water conservation nearly 70–80%. So, it has priority to be used in thermal power plants, especially those built in regions which are short for water and rich for coal, e.g., North China areas (Xu et al. 2015; Li et al. 2008). With the improvement of energy saving and environment protection requirements, construction and operation of large capacity air-cooling units in thermal power plants are imperative to balance the increasing electricity consumption and water resource shortage.

Generally, the air-cooling structure in a large thermal power plant mainly consists of tubular reinforced concrete columns, spatial steel truss platform and A-shaped steel truss. Tubular reinforced concrete columns have the characteristics of thin-wall and great sizes, typically which are about 4 m in diameter, 0.3–0.5 m in thickness and 40 m in height. Spatial steel truss platform is 4–8 m high. Above the spatial steel truss platform, there is 10–15 m high A-shaped steel truss on which most equipment are installed. An air-cooling structure supports millions of tons of weight of the upper equipment.

Once the columns collapsed under earthquake, huge casualties and economic loss would be caused.

For common reinforced concrete members, lots of experimental investigations have been conducted (Nilson and Arthur 1968; Bathe and Ramaswamg 1979; Priestly and Benzoni 1996; Priestly et al. 1996; Lehman et al. 1995; Phan et al. 2007; Hindi 2005; Hindi et al. 2005; Wang et al. 2014; Afefy and El-Tony 2016; Jiong 2004; Li and Ren 2009; Elmorsi et al. 1998; Esmaeily and Shirmohammadi 2014; Shao et al. 2005; Zendaoui et al. 2016; Ren et al. 2010). Previous studies of reinforced concrete members have demonstrated that slender ratio, material property, axial compression ratio, reinforcement ratio, detailing art and stirrups played significant roles in the seismic behavior, especially the hysteretic performance of reinforced concrete members. While, the seismic performance, especially hysteretic performance of tubular reinforced concrete columns with thin-wall and great sizes used in air-cooling condenser structure has not yet been clarified so far.

Additionally, with the fast development of computer technology, numerical simulation methods play a more and more important role in the nonlinear analysis of structures. Popular finite element codes such as Abaqus, Ansys, OpenSees have been developed to simulate the structural responses of reinforced concrete members. For circular columns, Masukawa et al. (1999) investigated failure modes of hollow bridge piers using three-dimensional nonlinear finite element method. Shirmohammadi and Esmaeily (2015) proposed an analytical algorithm and confirmed its accuracy, and it was also used to perform a parametric study considering the effects of axial load variation and lateral force/displacement paths on the flexural strength and energy dissipation capacity of reinforced

---

School of Civil Engineering, Xi'an University of Architecture and Technology, No. 13, Yanta Road, Xi'an 710055, Shaanxi, China.

\*Corresponding Author; E-mail: xuyazhou@xauat.edu.cn

Copyright © The Author(s) 2017. This article is an open access publication

concrete columns. Kim et al. (2012) proposed a framework for assessment of the seismic performance of hollow reinforced concrete and prestressed concrete bridge columns.

The primary objective of this study is to investigate the seismic response and failure modes of tubular reinforced concrete columns by pseudo-static testing, and develop a simple, yet reasonably accurate finite element model to predict the nonlinear cyclic response of this kind of columns. Accuracy of the FEM model was validated against experimental results. Furthermore, based on the validated analytical model, a parametric study was finally carried out to clarify the effect of axial compression ratio and longitudinal reinforcement on the ultimate strength, ductility and energy dissipation capacity.

## 2. Experimental Program

The prototype air-cooling structure was located in Jinjie thermal power plant, whose full-scale tubular reinforced concrete columns are 24.6 m high with outer diameter of 4 m and thickness of 0.4 m, as shown in Fig. 1. As well-



Fig. 1 The prototype air-cooling structure.

known, axial compression ratio and reinforcement ratio play an important role on the seismic performance of concrete structures. In consideration of the characteristics of thin wall and large size for the tubular reinforced concrete columns, reinforcement ratio, thickness and axial force were chosen as the test variables. The axial force exerted on the specimen was determined based on the axial compression ratio of the prototype air-cooling structure columns under different combined load cases. Confined to the laboratory condition and consideration of economy, four 1/8 scaled specimens were fabricated and tested through pseudo-static testing in present works. According to the similarity law, four scaled specimens are 3.07 m high with outer diameter of 0.5 m.

### 2.1 Details of Specimens

#### 2.1.1 Determination of the Axial Compression Ratio

The axial force exerted on the specimen was determined based on the axial compression ratio of the prototype air-cooling structure columns under different combined load cases (Table 1).

In Table 1, DL is dead load, LL is live load, S is snow load, W is wind load and EQ is earthquake action. X and Y are the directions of the earthquake. According to the Table 1, 0.09, 0.15, 0.20 was taken for the test.

#### 2.1.2 Determination of Specimen Section

The cross section of the prototype column is  $4000 \times 4000$  mm while the cross section of the scaled column is  $500 \times 500$  mm according to the 1/8 scaled ratio. In order to investigate whether the change of wall thickness will influence the seismic performance of columns, the cross sections of  $500 \times 70$  mm and  $500 \times 100$  mm were designed. 15, 16, 22, 20 longitudinal steel bars with the

Table 1 Axial compression ratio of full-scale tubular reinforced concrete columns under different combined load cases.

Combined load cases	Maximum value		Minimum value	
	Axial force/kN	Axial compression ratio	Axial force/kN	Axial compression ratio
1.35DL + 1.5LL	24244.08	0.20	16045.09	0.12
1.35DL + 1.5 W(+X)	22306.86	0.17	13237.49	0.10
1.35DL + 1.5 W(+Y)	20561.50	0.16	13638.27	0.10
1.35DL + 1.35LL + 1.35S + 1.35 W(+X)	22760.59	0.17	15767.53	0.12
1.35DL + 1.35LL + 1.35S + 1.35 W(+Y)	24396.77	0.20	15981.41	0.12
1.2DL + 0.55LL + 0.7S + 1.0EQ(+X)	19825.45	0.15	13119.34	0.10
1.2DL + 0.55LL + 0.7S + 1.0EQ(+Y)	19819.36	0.15	13155.10	0.10
1.0DL + 1.0LL + 1.0S + 1.0 W(+X)	16859.70	0.13	11679.65	0.09
1.0DL + 1.0LL + 1.0S + 1.0 W(+Y)	18071.68	0.14	11838.08	0.09

diameter of 10 mm were used in the Tube1–Tube4, respectively. The circular stirrup was 8 mm in diameter and arranged with the spacing of 200 mm except for the top and bottom 500 mm of the columns, in which the spacing is 100 mm. Experimental yielding strength values of steel reinforcement and circular stirrup were 461.7 and 315.8 MPa.

### 2.1.3 Determination of the Axial Force

The axial force  $N$  was calculated by the following equation:

$$N = n f_c^s A \quad (1)$$

where  $n$  denotes the axial compression ratio,  $f_c^s$  is measured value of concrete compression strength and  $A$  is the area of cross section. Take Tube1 for example,  $N = n f_c^s A = 0.09 \times 28.88 \times 70650 = 180$  kN. The detailed dimensions and material properties are listed in Table 2, where  $f_{cuk}$  and  $f_{ck}$  and

$f_{ck}$  denote the cubic compression strength of concrete and prism compression strength of concrete, respectively.

The spacing of the specimens is shown in Fig. 2. The detailed dimensions and material properties are listed in Table 2, where  $f_{cuk}$  and  $f_{ck}$  denote the cubic compression strength of concrete and prism compression strength of concrete, respectively.

### 2.2 Test Setup and Instrumentation Layout

Four specimens were tested by an electro-hydraulic servo system of MTS. The testing setup is manifested in Fig. 3.

### 2.3 Loading System

During the testing process, the vertical axial force was firstly applied on the top of the specimens with specified values and kept constant. The cyclic lateral displacement was then exerted to simulate seismic action through displacement control method. The specific loading system is as follows:

Table 2 Details of specimens.

Specimen	Diameter (mm)	Thickness (mm)	Axial Force (kN)	Axial compression ratio	$f_c^s$ (MPa)	$f_{cuk}$ (MPa)	$f_{ck}$ (MPa)	Reinforcement (mm <sup>2</sup> )
Tube1	500	50	180	0.09	28.88	38.1	25.5	1178 (15C10)
Tube2	500	100	360	0.09	31.92	42.0	28.1	1257 (16C10)
Tube3	500	50	434	0.20	27.36	36.0	24.1	1728 (22C10)
Tube4	500	70	422	0.15	34.96	46.4	31.0	1571 (20C10)

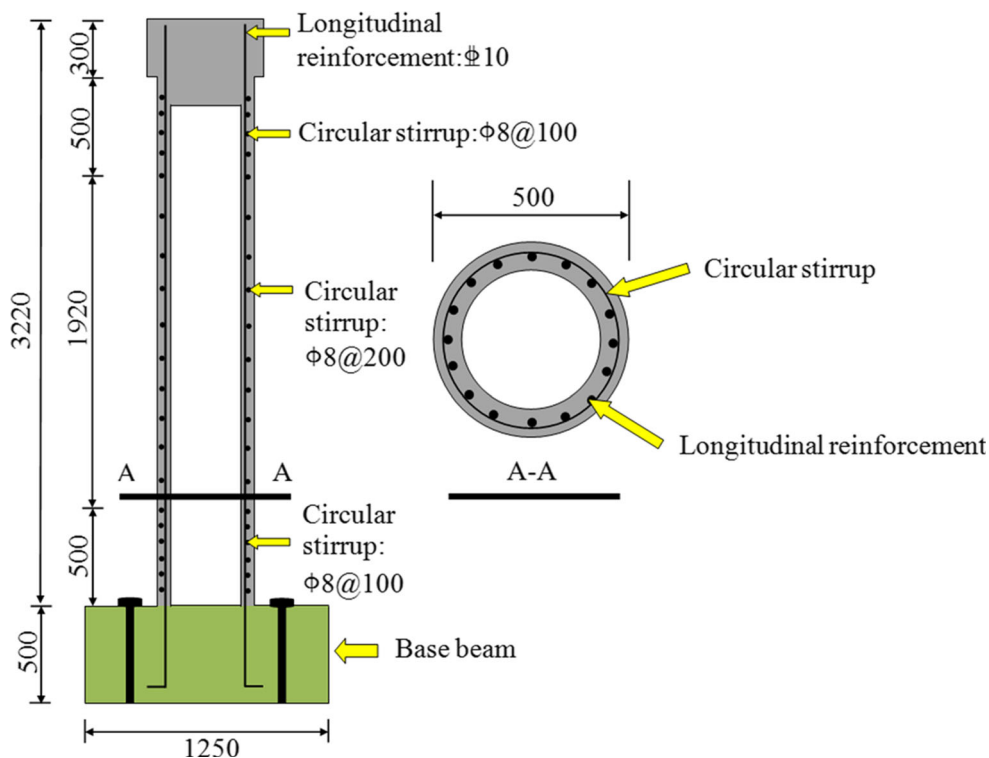


Fig. 2 Dimensions of specimens.

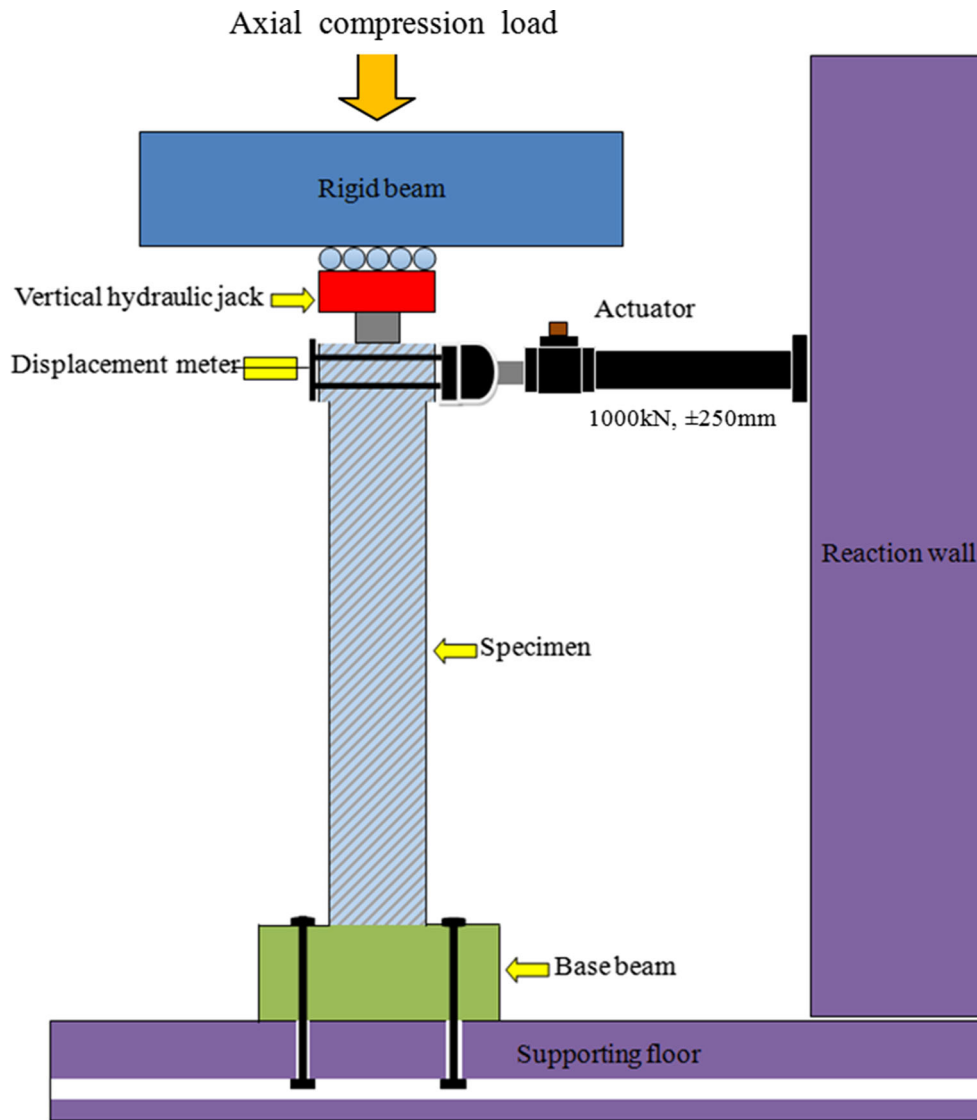


Fig. 3 Schematic of testing setup.

Table 3 Loading system of Tube 1.

Vertical axial force 180 kN				
	Target displacement (mm)	Displacement increment (mm)	Cycle number	Loading rate (mm/s)
1	3	1	1	0.2
2	7	2	2	0.5
3	13	3	2	0.5
4	22	3	3	0.5
5	37	3	3	1.0
6	79	6	3	1.0

### 2.3.1 Axial Compression Load

- (1) A 3-mm initial cyclic lateral displacement was exerted through the MTS actuator at first. Then, the value of the target displacement increased with increment of 1 mm each cyclic until visible cracks were observed on the specimens during the loading system.
- (2) The displacement increment value and the cycle number then increased to 2 mm and 2 times during the loading process until the specimen yielded. The yield point of the specimen was determined according to the load–displacement curve. 1000kN, ± 250 mm.

**Table 4** Loading system of Tube 2.

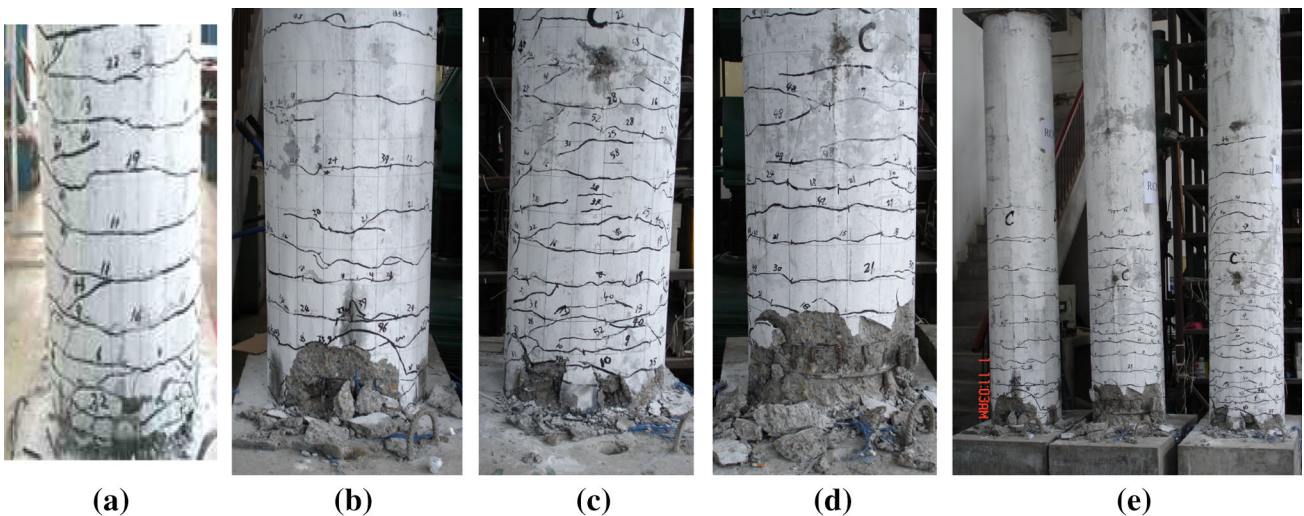
Vertical axial force 360 kN				
	Target displacement (mm)	Displacement increment (mm)	Cycle number	Loading rate (mm/s)
1	3	1	1	0.2
2	9	1	2	0.4
3	15	3	3	0.5
4	39	6	3	0.5
5	63	6	3	0.8
6	69	9	3	1.0

**Table 5** Loading system of Tube 3.

Vertical axial force 434 kN				
	Target displacement (mm)	Displacement increment (mm)	Cycle number	Loading rate (mm/s)
1	3	1	1	0.2
2	10	3	2	0.5
3	34	6	3	1.0

**Table 6** Loading system of Tube 4.

Vertical axial force 420 kN				
	Target displacement (mm)	Displacement increment (mm)	Cycle number	Loading rate (mm/s)
1	3	1	1	0.2
2	12	3	2	0.5
3	30	6	3	1.0
4	48	9	3	1.0
5	75	12	3	1.0

**Fig. 4** Failure modes of the specimens. a Tube 1. b Tube 2. c Tube 3. d Tube 4. e Tube 2–Tube 4.

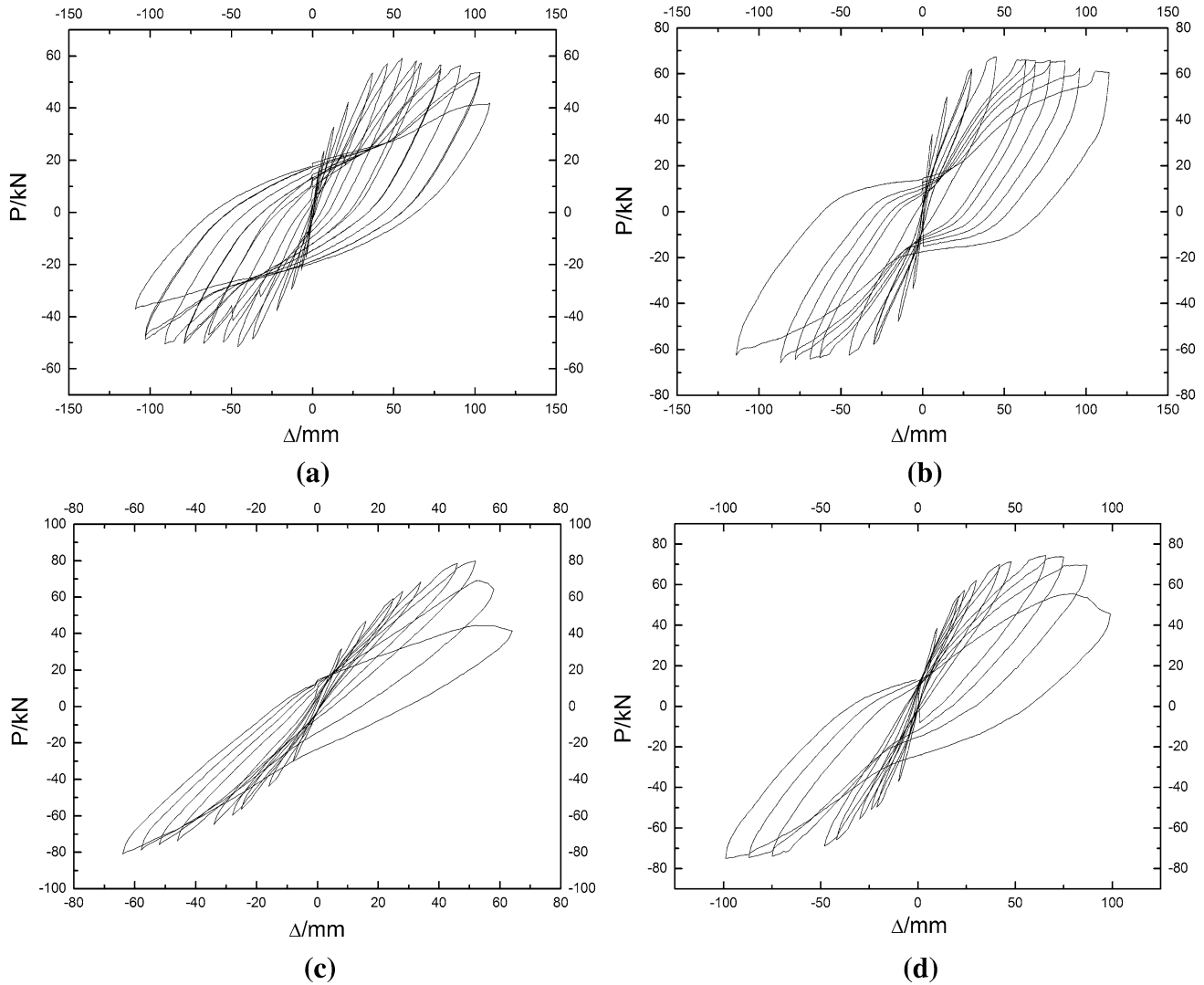


**Fig. 5** Hysteretic curves of lateral displacement-load. a Tube 1. b Tube 2. c Tube 3. d Tube 4.

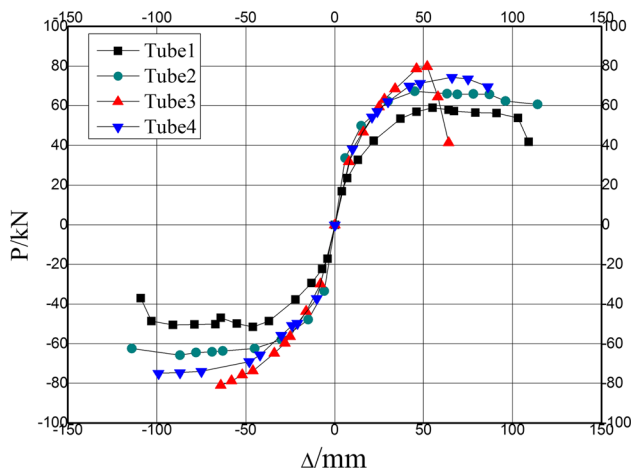


**Fig. 6** Skeletons of the lateral displacement-load hysteretic curves.

- (3) The target displacement and the cycle number were next adjusted according to the yield displacement. The displacement increment was multiples of the yield displacement. When the bearing capacity of a specimen

dropped to 85% of its ultimate load, the loading process was terminated.

The detailed loading procedures of each specimen are listed in Table 3, 4, 5 and 6.

### 3. Experimental Results And Specimen Behavior

#### 3.1 Failure Mode

The experimental crack distributions of four specimens are shown in Fig. 4. For Tube 1, when the top lateral displacement reached 4 mm, the visible bending cracks occurred 50 mm away from the bottom of the column. Then, the existing cracks continued to widen and extend while new cracks successively appeared. When the lateral displacement at the top of Tube 1 was 115 mm, large pieces of cover concrete at the bottom of the column spalled, longitudinal reinforcement buckled and bearing capacity dropped sharply, which indicated the specimen was severely damaged. The failure phenomena of Tube2–Tube4 are not repeated here due to the similarity to Tube 1.

**Table 7** Characteristic points of the skeleton curves.

Specimen	Crack point		Yielding point		Ultimate point		Ductility coefficient
	Displacement (mm)	Load (kN)	Displacement (mm)	Load (kN)	Displacement (mm)	Load (kN)	
Tube1	4.0	17.0	23.3	44.2	115.0	59.1	4.94
Tube2	6.0	33.6	16.0	51.0	114.0	67.4	7.13
Tube3	8.0	31.8	27.5	62.5	64.0	79.8	2.33
Tube4	10.0	38.4	22.8	56.2	99.0	74.4	4.34

As shown in Fig. 4, it was observed that the scope of cracks appearance can reach 3/4 of the column height. The crack distribution of the tubular columns demonstrates that in comparison to the conventional circular columns there is need for more zones with dense stirrups to improve the ductility of the columns.

**3.2 Lateral Load versus Displacement Relationship**

Experimental hysteretic curves of four specimens are shown in Fig. 5. It can be found that the tubular reinforced concrete columns show typically hysteretic features of reinforced concrete columns. It means, the load–displacement curves are nearly straight before yielding. With the development of cracks, the load–displacement curves show the feature of degradations of strength and stiffness and “pinching” effect. As shown in Fig. 5c, Tube 3 exhibits poorer ductility due to its higher axial compression ratio compared with other columns.

The skeleton curves of four specimens are shown in Fig. 6. The characteristic points, including crack load and displacement, yielding displacement and load, ultimate load and ultimate displacement, are listed in Table 7. The cracking loads were observed and recorded when initial

cracks occurred while the corresponding displacements were named crack displacement. The yielding points could be obtained by using the modified general yield bending moment method. The peak value of a skeleton curve was defined as ultimate load, while the displacement value corresponding to 0.85 times of the ultimate load on the skeleton curve was specified as ultimate displacement.

**3.3 Calculation of Normal Section Strength**

According to the Code for design of concrete structures of China, for ring-shaped section eccentric compression members (Fig. 7) with longitudinal steel reinforcements uniformly provided along the periphery, the normal section compressive load-bearing capacity may conform to the following stipulations:

$$N \leq \alpha \alpha_1 f_c A + (\alpha - \alpha_t) f_y A_s \tag{2}$$

$$N e_i \leq \alpha_1 f_c A (r_1 + r_2) \frac{\sin \pi \alpha}{2\pi} + f_y A_s r_s \frac{(\sin \pi \alpha + \sin \pi \alpha_t)}{\pi} \tag{3}$$

The coefficient and eccentricity in above equations shall be calculated according to the following equations:

$$\alpha_t = 1 - 1.5\alpha \tag{4}$$

$$e_i = e_0 + e_a \tag{5}$$

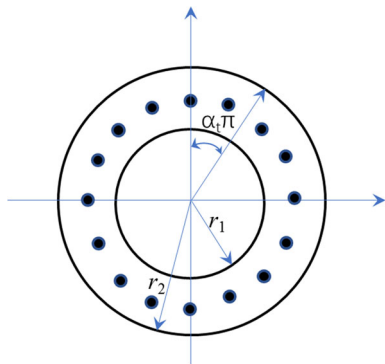


**Fig. 7** Ring-shaped section eccentric compression members.

where  $A$  area of ring-shaped section;  $A_s$  area of section for all longitudinal ordinary steel reinforcements;  $r_1, r_2$  interior, exterior radius of ring-shaped section respectively;  $r_s$  radius of circumference, where the centroid of longitudinal ordinary steel reinforcements is situated;  $e_0$  eccentricity of axial compression force to centroid of section;  $e_a$  additional eccentricity;  $\alpha$  value for ratio of sectional area of concrete in compression zone to full sectional area of concrete;  $\alpha_t$  value for ratio of sectional area of longitudinal tension steel reinforcements to area of all longitudinal steel reinforcements.

**Table 8** Comparison of the ultimate bending moment through the method in the code and test result.

Specimen	Tube 1	Tube 2	Tube 3	Tube 4
Calculation method (kN m)	141	170	212	206
Test result (kN m)	181.4	206.9	245.0	228.4
D-value (%)	22	17.5	13.5	9.8

The calculation method specified in Code for design of concrete structures of China is suitable for the conventional circular columns with large ratio of thickness to diameter. Tubular reinforced concrete columns have the characteristics of small ratio of thickness to diameter due to the thin-wall and great sizes. It is necessary to verify the applicability of the method in the code. The ultimate bending moment obtained through the method in the code and the pseudo-static test are shown in Table 8.

The comparison in Table 8 shows that it is conservative to calculate the normal section bearing capacity through the method proposed by the Code for design of concrete structures of China.

#### 4. Numerical Simulation

OpenSees is an object-oriented framework for building models of structural and geotechnical systems to perform

nonlinear analysis. OpenSees supports a wide range of simulation applications in earthquake engineering and its good nonlinear numerical simulation precision has been widely confirmed.

##### 4.1 Finite Element Model

Here, the tubular reinforced concrete columns were simulated with the fiber model. The finite element models are fixed at the bottom ends, while free at the top ends, see in Fig. 8. The fiber section command was used to construct a uniaxial fiber object and add it to the section. The cross section of specimens could be divided into several small patches. According to the plane section assumption, OpenSees automatically calculates the strain of each fiber and ensure forces of the cross section keeping balance through iterative treatment. To model the whole columns, a nonlinear beam-column element based on the non-iterative force formulation was employed while considering the spread of plasticity along the element.

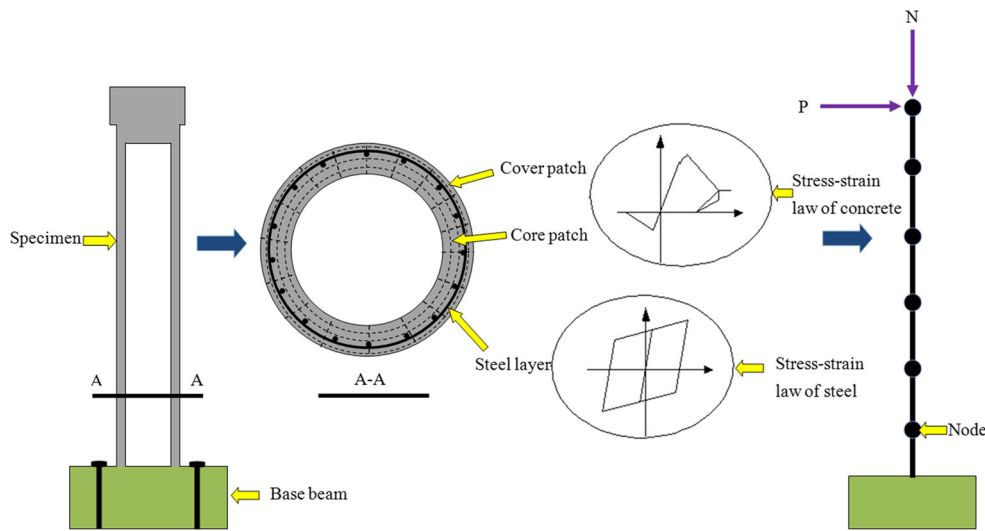


Fig. 8 Finite element models.

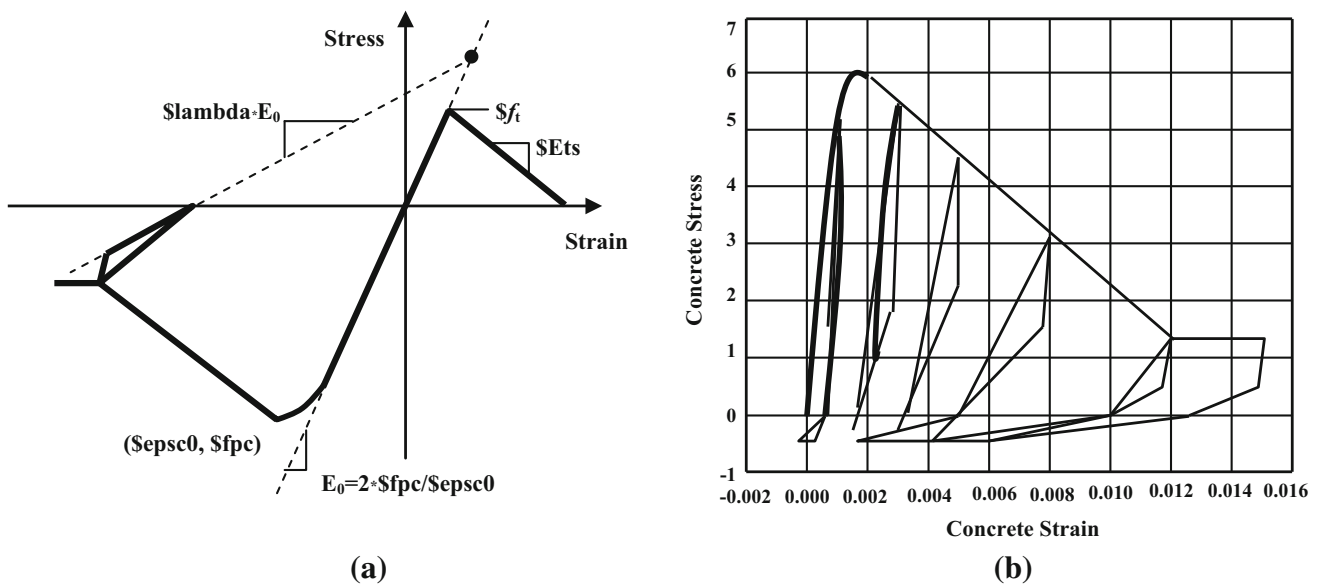


Fig. 9 Concrete02 material model in OpenSees. a Monotone stress–strain relationship. b Hysteretic stress–strain relationship.

## 4.2 Constitutive Laws of Steel and Concrete

As well-known, it is crucial to select a reasonable concrete and steel material models in the nonlinear finite element simulation. Three concrete stress–strain material models are available in the OpenSees code, i.e., Concrete01, Concrete02 and Concrete03. Concrete02, a linear tension softening material model in which the compression skeleton curve is specified by the Kent-Park stress–strain relationship (Kent and Park 1971), was used to construct a uniaxial concrete material with a linear tension softening branch.

Since the restraint effect of stirrups on concrete was so small that it could be ignored and concrete was treated as an unconfined material according to the researches of Mander et al. (1998) and Scott et al. (1982).

Figure 9 displays the monotone and hysteretic stress–strain rules of Concrete02. The uniaxial compressive stress–strain relationship of Concrete02 is regulated as

$$f = Kf_{co} \left[ 2 \left( \frac{\varepsilon}{\varepsilon_{cc}} \right) - \left( \frac{\varepsilon}{\varepsilon_{cc}} \right)^2 \right] \quad (0 \leq \varepsilon \leq \varepsilon_{cc}) \quad (6)$$

$$f = Kf_{co} [1 - Z(\varepsilon - \varepsilon_{cc})] \quad (\varepsilon_{cc} \leq \varepsilon \leq \varepsilon_{cu}) \quad (7)$$

$$f = 0.2Kf_{co} \quad (\varepsilon_{cu} \leq \varepsilon) \quad (8)$$

where  $f$ ,  $\varepsilon$ ,  $f_{co}$ ,  $\varepsilon_{cc}$  are stress, strain, axial compressive strength and peak strain, respectively. The slope of the strain softening part can be written as

$$z = \frac{0.5}{\frac{3+0.29f_{co}}{145f_{co}-1000} + 0.75\rho_s \sqrt{\frac{h'}{S_h}} - 0.002K} \quad (9)$$

where  $h'$  and  $S_h$  are the width of core concrete and stirrup spacing.  $K$  denotes the coefficient of concrete strength increased by the cyclic-hoop effect.

$$K = 1 + \frac{\rho_s f_{yh}}{f_{co}} \quad (10)$$

$$\varepsilon_{cc} = 0.002K \quad (11)$$

In Eq. (10),  $\rho_s$  and  $f_{yh}$  denote the volumetric percentage of stirrups and corresponding yielding strength. When  $K$  equals to one, Eqs. (6)–(11) are considered as the stress–strain relationship of unconstrained concrete. In addition, the uniaxial tension stress–strain relationship of Concrete02 is regulated as

$$\sigma_c = E_c \varepsilon_c \quad (\varepsilon_c \leq \varepsilon_{0t}) \quad (12)$$

$$\sigma_c = f_t \left[ 1 - \mu \left( \frac{\varepsilon_c}{\varepsilon_{0t}} - 1 \right) \right] \quad (\varepsilon_{0t} \leq \varepsilon_c \leq \varepsilon_{cr}) \quad (13)$$

$$\sigma_c = 0 \quad (\varepsilon_{cr} \leq \varepsilon_c) \quad (14)$$

$$\varepsilon_{0t} = \frac{f_t}{E_c} \quad (15)$$

where  $E_c$  and  $f_t$  denote the initial elastic modulus and axial tensile strength of concrete.  $\mu$  is the tension hardening coefficient.

There are two steel stress–strain material models in OpenSees: Steel01 and Steel02. Here, Steel02 material command is implemented as the constitutive law of steel. It was originally suggested by Menegotto and Pinto (1973). Then, this model was modified and the influence of strain hardening was taken into account. Since the stress–strain relationship of Steel02 is expressed in an explicit form, so it has high computational efficiency. Lots of simulation results have demonstrated its good consistency. Figure 10 shows the monotonic and hysteretic stress–strain curves of Steel02.

The Menegotto-Pinto stress–strain relationship can be expressed as

$$\sigma^* = b \cdot \varepsilon^* + \frac{(1-b) \cdot \varepsilon^*}{(1 + \varepsilon^{*R})^{1/R}} \quad (16)$$

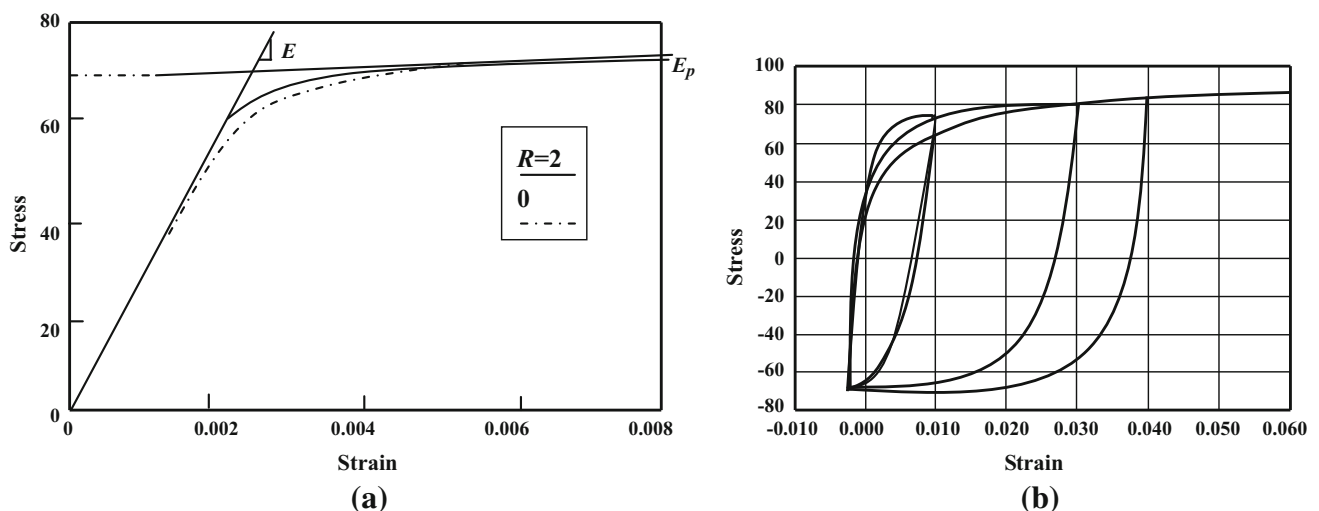


Fig. 10 Steel02 material model of OpenSees. a Monotonic stress–strain curve. b Hysteretic stress–strain curve.

where:

$$\varepsilon^* = \frac{\varepsilon - \varepsilon_r}{\varepsilon_0 - \varepsilon_r} \quad (17)$$

$$\sigma^* = \frac{\sigma - \sigma_r}{\sigma_0 - \sigma_r} \quad (18)$$

$$b = \frac{E_1}{E_0} \quad (19)$$

Equations (16)–(19) represents a curved transition from one straight line asymptote ( $E_0$ ) to another ( $E_1$ ).  $b$  is a parameter which reflects the strain-hardening ratio of steel. Figure 11 demonstrates the definition of points such as  $(\sigma_0, \varepsilon_0)$  and  $(\sigma_r, \varepsilon_r)$ .  $(\sigma_0, \varepsilon_0)$  denotes stress, strain at the point where the initial tangent and the asymptotes of the curve meet.  $(\sigma_r, \varepsilon_r)$  denotes stress, strain at the last reversal point. Parameter  $R$  can reflect the Bauschinger effect of reinforcement and have an influence on the shape of transition curves.  $R$  can be calculated through equation  $R(\xi) = R_0 - (a_1 \cdot \xi)/(a_2 + \xi)$ , where  $R_0$  is the initial value of parameters  $R$  for the first loading. Values of  $a_1, a_2, R_0$ , can be obtained by experimental results.

In order to take the isotropic hardening effect into account and improve the Menegotto-Pinto model, Filippou et al. (1983) proposed that the linearized yielding asymptote should be adopted. The translation value can be then written as

$$\frac{\sigma_{st}}{f} = a_3 \cdot \left( \frac{\varepsilon_{smax}}{\varepsilon_y} - a_4 \right) \quad (20)$$

where  $\varepsilon_{smax}, \varepsilon_y, f_y$  are the maximum absolute value of reverse strain, yielding strain and yielding stress of steel. Parameters,  $a_3$ , and  $a_4$ , can be identified in terms of experimental results.

$R_0$  is the parameter which determines the transition from elastic to plastic branches and the recommended values are 10–20 according to the OpenSees user's manual and

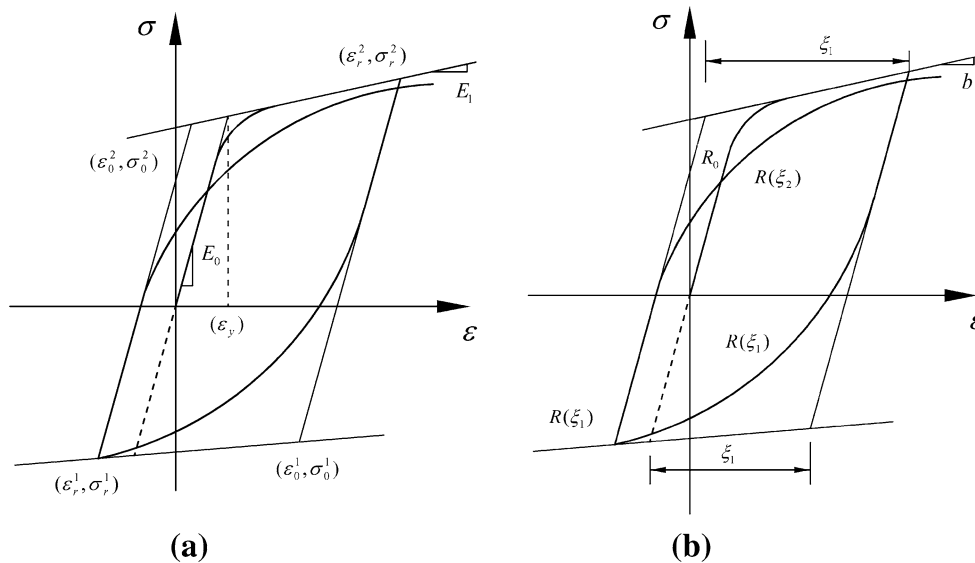


Fig. 11 Menegotto-Pinto model for steel. a Menegotto-Pinto stress–strain relationship of steel. b Definition of parameter R.

examples primer (Mazzoni and McKenna 2003; Mazzoni et al. 2003).  $a_1$  is the isotropic hardening parameter which is related to the increase of compression yield envelope after a plastic strain of  $a_2 \cdot f_y / E_0$ .  $a_2$  and  $a_4$  are the isotropic hardening parameters.  $a_3$  is the isotropic hardening parameter which is related to the increase of tension yield envelope after a plastic strain of  $a_4 \cdot f_y / E_0$ . In order to determine these parameters in the absence of detailed testing results of the materials, it is necessary to identify the values of the parameters in a reasonable range during the simulation process, so that the simulation results are in good accordance with the experimental results of the columns. Then, the verified FEM models can be employed to study the influence of the axial force, and so on.

For finite element simulations, the axial force was firstly applied and the displacement on the top node was then exerted to simulate lateral loading. Finally, Newton algorithm and norm displacement increment method were adopted to find numerical solutions.

### 4.3 Model Validation

Figure 12 shows the comparison of the experimental and numerical hysteretic curves. It can be found that the OpenSees models can capture the main hysteretic features of tubular reinforced concrete columns, and the simulation results match well with the experimental ones as a whole. Taking Tube 1 for instance, the experimental ultimate load and ultimate displacement are 59.1kN and 23.3 mm, the numerical results are 58.4kN and 26.0 mm.

However, the predicted hysteretic curves by OpenSees are much more plump and the pinching effect is not obvious as the experimental one. Adopting plane section assumption and no consideration in bond-slip between concrete and steel should be the main reason. In fact, due to the uncertainty of the experiment and deficiency of numerical models, it is

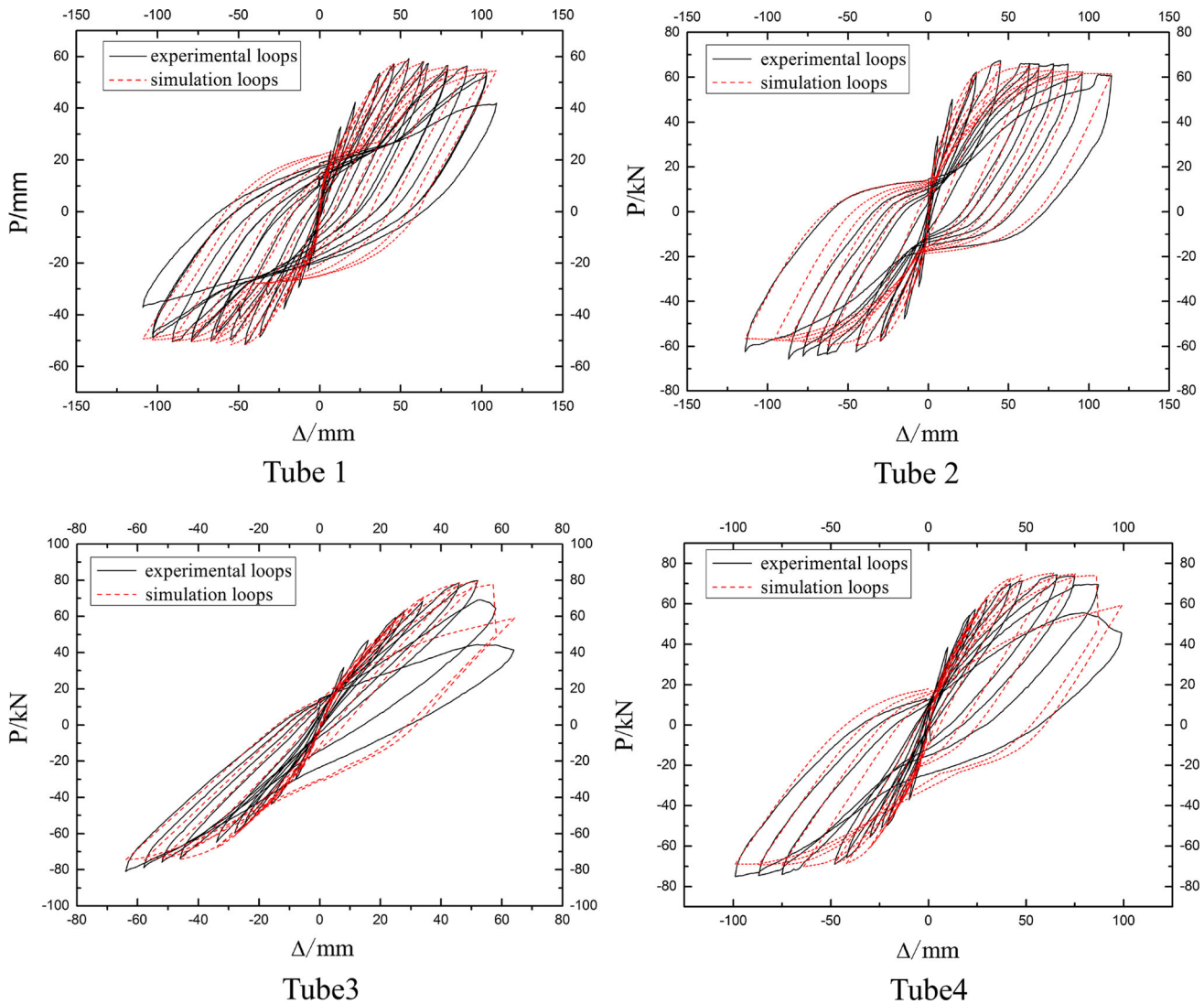


Fig. 12 Comparison of experimental and simulation hysteretic curves.

often difficult to accurately simulate the declining branches and pinching effect of experimental results.

## 5. Parametric Studies

As well-known, ductility and energy dissipation capacity are mainly influenced by parameters such as ratio of axial compression and longitudinal reinforcement. Owing to the limited number of specimens, numerical simulation was then performed to investigate the influence of parameters based on the validated finite element models.

### 5.1 Influence of Axial Compression Ratio

In order to investigate the influence of axial compression ratio on the bearing capacity, energy dissipation capacity and stiffness of columns, the magnitude of axial load was adjusted. New models were designed on the basis of Tube2 (3.07 m high, diameter 500 mm, wall thickness 100 mm) and values of the axial compression ratio were 0.14, 0.20, 0.25, 0.30, 0.35, 0.40, respectively. The horizontal

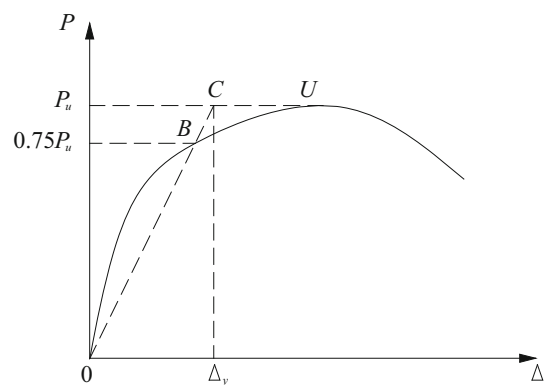
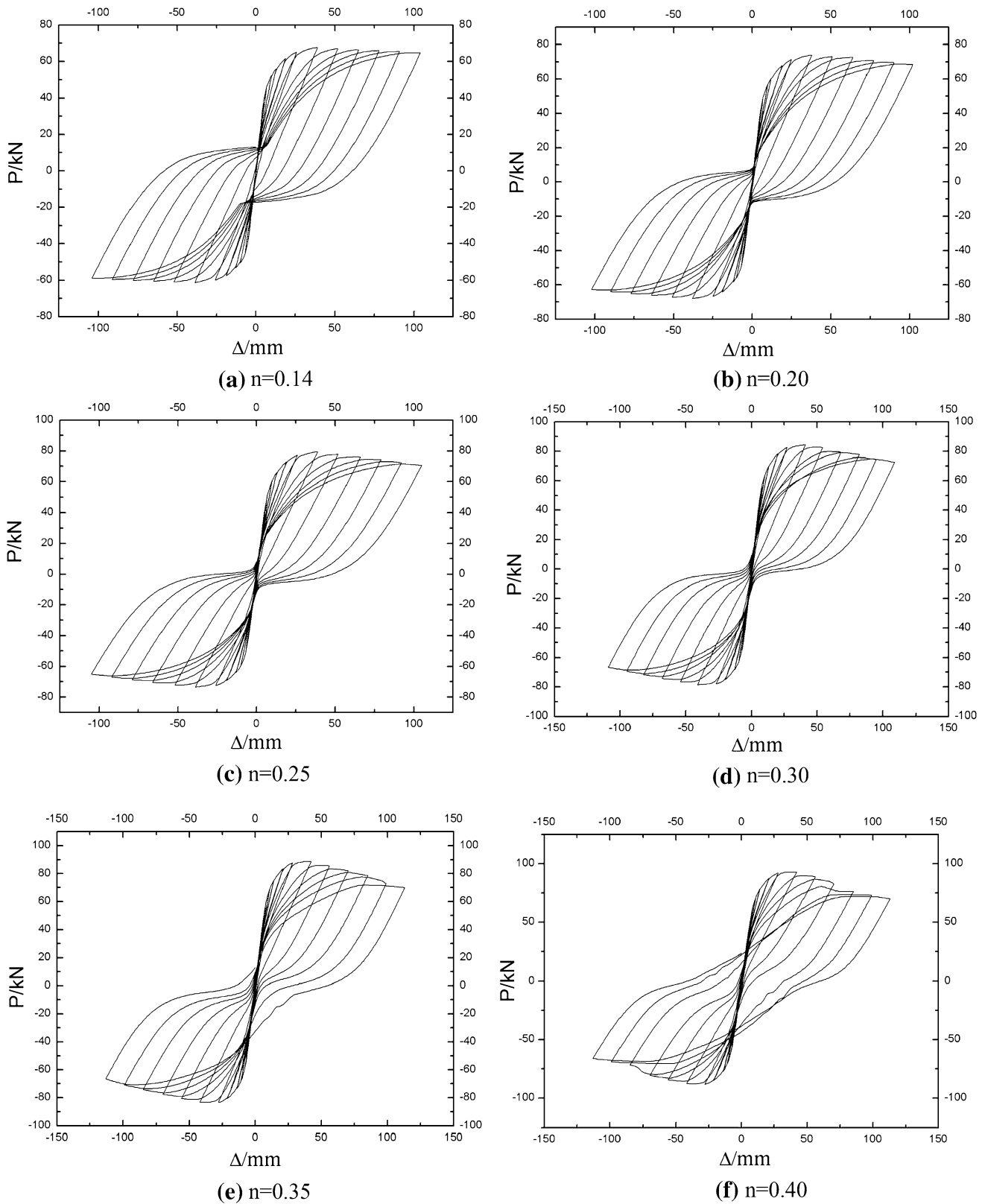


Fig. 13 Park method.

displacement on the top of the column was in accordance with the sequence of  $0.2\Delta_y$ ,  $0.4\Delta_y$ ,  $0.6\Delta_y$ ,  $0.8\Delta_y$ ,  $\Delta_y$ ,  $1.5\Delta_y$ ,  $2\Delta_y$ ,  $3\Delta_y$ ,  $4\Delta_y$ ,  $5\Delta_y$ ,  $6\Delta_y$ ,  $7\Delta_y$ ,  $8\Delta_y$ . Here,  $\Delta_y$  is the equivalent yield displacement which can be calculated by the Park method (Fig. 13).



**Fig. 14** Hysteretic curves with different axial compression ratio for Tube2.

### 5.1.1 Hysteretic Loops and Skeleton Curves

The simulation results of the hysteretic loops and skeleton curves are shown in Figs. 14 and 15.

It is obvious that with the increase of axial pressure ratio, the corresponding maximum load also increases. However,

as the axial compression ratio is exceedingly large, the ultimate load increases slowly.

It also can be found that the smaller axial compression ratio is, the less the skeleton curve declines. Therefore, taking the importance of tubular reinforced concrete columns into

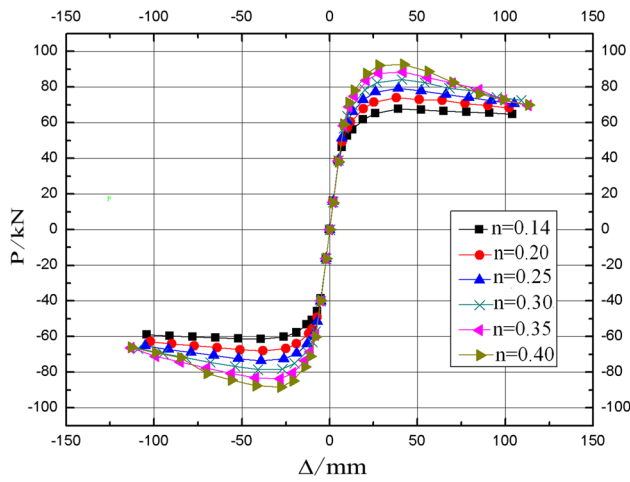


Fig. 15 Skeleton curves with different axial compression ratio for Tube2.

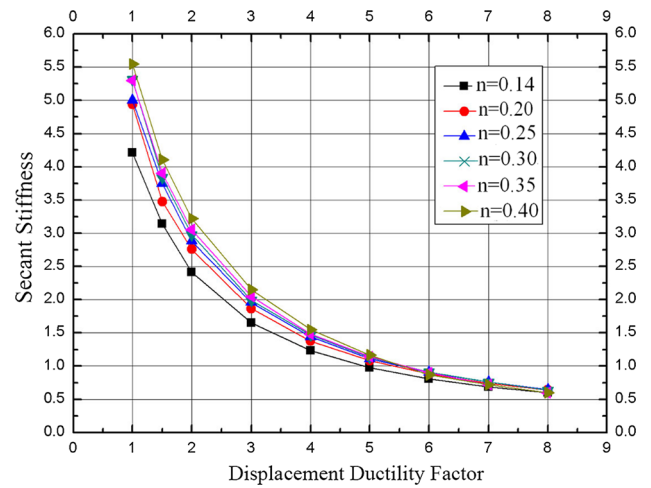


Fig. 17 The relationship between displacement ductility factor and the stiffness degradation.

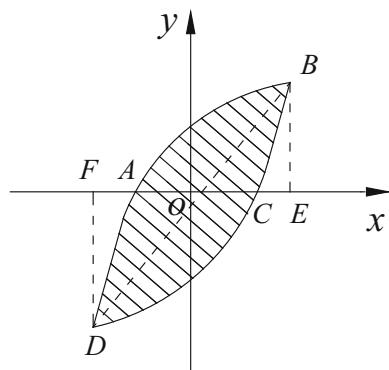


Fig. 16 Parameters meanings of Eqs. (21) and (22).

account, it is indispensable to restrict the maximum value of the axial compression ratio to ensure the seismic performance.

### 5.1.2 Energy Dissipation Capacity

Energy dissipation capacity of structures or components is often measured by the energy dissipation coefficient  $E$  and equivalent viscous damping coefficient  $h_e$ . These two coefficients are defined as

$$E = \frac{S_{(ABC+CDA)}}{S_{(OBE+ODF)}} \quad (21)$$

$$h_e = \frac{1}{2\pi} \times \frac{S_{(ABC+CDA)}}{S_{(OBE+ODF)}} \quad (22)$$

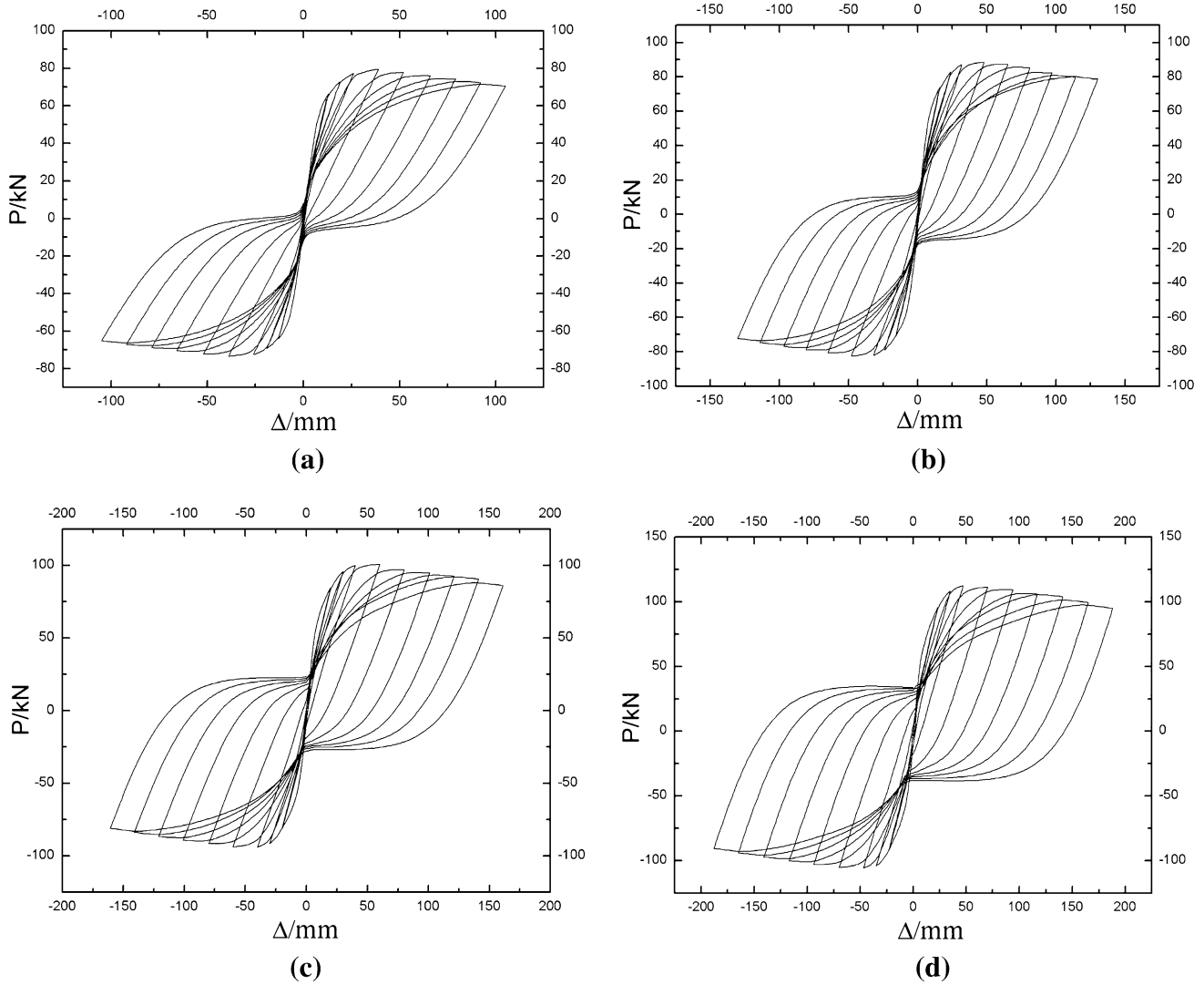
Meanings of the parameters in above formulas are shown in Fig. 16.

Based on the simulation results of cyclic loading, energy dissipation coefficient  $E$  and equivalent viscous damping coefficient  $h_e$  with different axial compression ratio for Tube2 during yielding stage and limit stage can be calculated through Eqs. (21) and (22), see in Table 9.

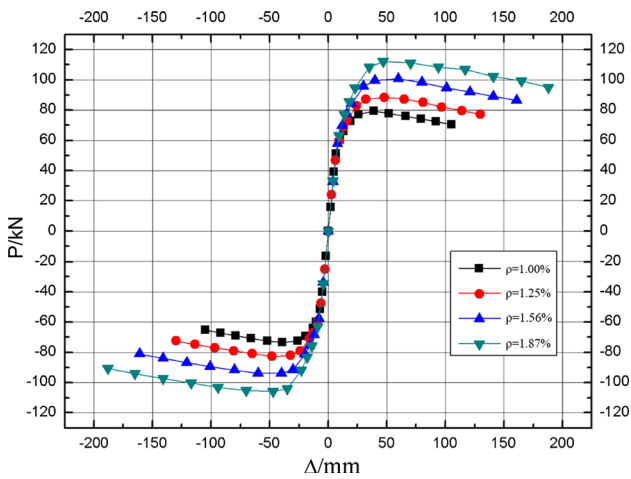
From Table 9, it is easy to find that the equivalent viscous damping coefficient  $h_e$  and energy dissipation coefficient  $E$  in the limit stage are bigger than the yielding stage. As expected, with the increase of axial compression ratio, the equivalent viscous damping coefficient  $h_e$ , energy dissipation coefficient  $E$  and energy dissipation capacity of the columns decreases gradually. This is mainly because that as a large eccentric compression member, the height of compression zone for tubular reinforced columns is relatively small which is in favor of energy dissipation capacity and ductility. If the axial compression ratio increases, the height

Table 9  $E$  and  $h_e$  with different axial compression ratio for Tube2.

Axial compression ratio	Yielding stage				Limit stage			
	$S_{(ABC+CDA)}$ (kN mm)	$S_{(OBE+ODF)}$ (kN mm)	$E$	$h_e$	$S_{(ABC+CDA)}$ (kN mm)	$S_{(OBE+ODF)}$ (kN mm)	$E$	$h_e$
n = 0.14	198.3115	715.3398	0.2772	0.0441	1517.5058	2506.6128	0.6054	0.0964
n = 0.20	170.1344	648.1608	0.2625	0.0418	1446.9708	2442.3400	0.5925	0.0943
n = 0.25	181.8989	847.2856	0.2147	0.0342	1486.9411	2975.6870	0.4997	0.0795
n = 0.30	189.2101	898.9050	0.2105	0.0335	1682.7438	3382.3282	0.4975	0.0792
n = 0.35	211.7772	1040.3058	0.2036	0.0324	1784.3739	3604.5775	0.4950	0.0788
n = 0.40	215.8960	1086.6254	0.1987	0.0316	844.4114	2628.8536	0.3212	0.0511



**Fig. 18** Hysteretic loops with different longitudinal reinforcement ratio for Tube2 **a**  $\rho = 1.00\%$  **b**  $\rho = 1.25\%$  **c**  $\rho = 1.56\%$  **d**  $\rho = 1.87\%$ .



**Fig. 19** Skeleton curves with different longitudinal reinforcement ratios for Tube2.

of relative compression zone will increase as well which would weaken the ductility and energy dissipation performance of the columns. When the axial compression ratio is

too large, the tubular reinforced columns would become members with large compression zones, which deteriorates the energy dissipation capacity and ductility.

### 5.1.3 Stiffness

Stiffness degradation can reflect the capacity of resistance to lateral collapsing, which can be measured by secant stiffness. Secant stiffness is the ratio of peak load at each loading level and the associated displacements in positive and negative direction. It is calculated by the formula below

$$K_i = \frac{|+F_i| + |-F_i|}{|+X_i| + |-X_i|} \quad (23)$$

where  $F_i$  and  $X_i$  and are the peak load and peak displacement. The stiffness degradation of the specimens with different axial compression ratio for Tube2 is illuminated in Fig. 17.

One can find that values of the secant stiffness for the tubes with higher axial compression ratio are larger than the others. With the development of plastic deformation, the tendency of stiffness degradation gradually becomes

**Table 10**  $E$  and  $h_e$  with different longitudinal reinforcement ratios for Tube2.

Longitudinal reinforcement ratio (%)	Yielding stage				Limit stage			
	$S_{(ABC + CDA)}$ (kN mm)	$S_{(OBE + ODF)}$ (kN mm)	$E$	$h_e$	$S_{(ABC + CDA)}$ (kN mm)	$S_{(OBE + ODF)}$ (kN mm)	$E$	$h_e$
$\rho = 1.00$	181.8989	847.2856	0.2147	0.0342	1486.9411	2975.6128	0.4997	0.0795
$\rho = 1.25$	274.8453	1158.6722	0.2372	0.0378	2603.9790	4096.8782	0.6356	0.1012
$\rho = 1.56$	414.7068	1661.2259	0.2496	0.0397	4747.6610	5823.3371	0.8153	0.1298
$\rho = 1.87$	538.7275	2151.6598	0.2504	0.0398	7278.6079	7564.3521	0.9622	0.1531

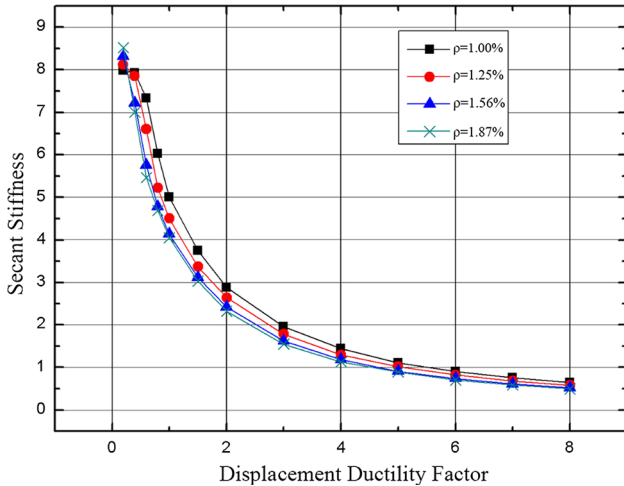


**Fig. 20** The relationship between the displacement ductility factor and stiffness degradation.

moderate. Figure 17 also shows that the tubes with different axial compression ratio share the same pattern of stiffness degradation.

## 5.2 Influence of Longitudinal Reinforcement

On the basis of Tube 2 and Tube 4, finite element models with different longitudinal reinforcement were established to study its influence on the bearing capacity, energy dissipation capacity and stiffness degradation. The longitudinal reinforcement ratios of these 4 models are 1.00, 1.25, 1.56, 1.87, respectively. The loading procedure is the same as mentioned above.

### 5.2.1 Hysteretic Loops and Skeleton Curves

The simulation results of the hysteretic loops and skeleton curves with different longitudinal reinforcement ratios are shown in Figs. 18, 19. The simulated results indicate that the ultimate load of tubular columns enhances obviously with the increase of longitudinal reinforcement ratio, which is also beneficial to seismic ductility.

### 5.2.2 Energy Dissipation Capacity

Table 10 shows the energy dissipation capacity of the tubes under different longitudinal reinforcement ratios.

Studies of energy dissipation coefficient  $E$  and equivalent viscous damping coefficient  $h_e$  suggest that  $E$  and  $h_e$  in yielding stage and limit stage become larger with the increase of longitudinal reinforcement ratio. This

demonstrates again that longitudinal reinforcement ratio is in favor of improving energy dissipation capacity of the tubular columns.

### 5.2.3 Stiffness

The stiffness degradation of the numerical specimens with different longitudinal reinforcement ratios for Tube2 is illuminated in Fig. 20. It can be seen that, within a certain range, increasing longitudinal reinforcement ratio could relieve stiffness degradation and improve the ductility of tubular columns.

## 6. Conclusions

In this study, a pseudo-static test and experimental results for four 1/8 scaled tubular reinforced concrete columns of air-cooling condenser structures are reported. Seismic behaviors, hysteretic properties and failure modes were evaluated based on experimental results. Then, finite element models using OpenSees were established to simulate their hysteretic loops. The constitutive laws in OpenSees, Steel02 and Concrete02, were chosen to model the behaviors of steel and concrete subjected cyclic loading. At last, numerical specimens were established to investigate the influence of axial compression ratio and longitudinal reinforcement ratio on bearing capacity of the columns.

From the results of the experimental and analytical studies, the following conclusions were reached:

- (1) Tubular reinforced concrete columns of air-cooling condenser structures exhibit a moderate ability of energy dissipation.
- (2) The predicted results obtained by the OpenSees finite element can reasonably capture the main features of the tubular reinforced concrete columns. Nevertheless, it is hard to accurately simulate the severe damage stage of the experimental results. Further researches are still needed to improve the accuracy and convergence for numerical simulations.
- (3) With the increase of axial pressure ratio, the corresponding maximum load also increases. But after the axial compression ratio reaches a certain value, the skeleton curves drop much more steeply and exhibits poor ductility. Besides, longitudinal reinforcement is indeed in favor of improving the seismic performance of the reinforced concrete tubular columns.

- (4) It is conservative to calculate the normal section bearing capacity through the method proposed by the Code for design of Concrete Structures of China. Besides, the crack distribution of the tubular columns demonstrates that in comparison to the conventional circular columns there is need for more zones with dense stirrups to improve the ductility of the columns.

## Acknowledgements

The support of the Natural Science Foundation of China (Grant No. 51478381,51578444) and Ministry of Education Plan for Yangtze River Scholar and Innovation Team Development (No. IRT13089) is acknowledged.

## Open Access

This article is distributed under the terms of the Creative Commons Attribution 4.0 International License (<http://creativecommons.org/licenses/by/4.0/>), which permits unrestricted use, distribution, and reproduction in any medium, provided you give appropriate credit to the original author(s) and the source, provide a link to the Creative Commons license, and indicate if changes were made.

## References

- Afey, H. M., & El-Tony, E. T. M. (2016). Simplified design procedure for reinforced concrete columns based on equivalent column concept. *International Journal of Concrete Structures and Materials*, 10(3), 393–406.
- Bathe, K. J., & Ramaswam, S. (1979). On three-dimensional nonlinear analysis of concrete structures. *Nuclear Engineering and Design*, 52(3), 843–855.
- Elmorsi, M., Kianoush, M. R., & Tso, W. K. (1998). Nonlinear analysis of cyclically loaded reinforced concrete structures. *ACI Struct*, 95(6), 725–739.
- Esmaily, A., Shirmohammadi, F. (2014). Performance and capacity assessment of reinforced concrete bridge piers considering the current load and resistance factor design provisions and plastic hinge length in Kansas. No. K-TRAN: KSU-11-5.
- Filippou, F. C., Povov, E. P., Bertero, V. V. (1983). Effects of bond deterioration on hysteretic behavior of reinforced concrete joints. EERC Report No. UCB/EERC-83/19, Earthquake Engineering Research Center, University of California, Berkeley.
- GB50010-2010, Code for design of concrete structures, Beijing: China Architecture and Building Press, 2010(only available in China).
- Hindi, R. (2005). Cross spirals reinforcement to confine reinforced concrete columns. US and International Patent Application, May 13.

- Hindi, R., Al-Qattawi, M., Elsharief, A. (2005). Influence of different confinement patterns on the axial behavior of RC columns. *Proceedings of the ASCE*, New York, US.
- Jiong, L. (2004). Applications and redevelopments of object-oriented and open-sourced program OpenSees on RC structure nonlinear analysis. PhD Thesis, Chongqing University, Chongqing, China.
- Kent, D. C., & Park, R. (1971). Flexural members with confined concrete. *ASCE*, 97(7), 1969–1990.
- Kim, T. H., Seong, D. J., & Shin, H. M. (2012). Seismic performance assessment of hollow reinforced concrete and prestressed concrete bridge columns. *International Journal of Concrete Structures and Materials*, 6(3), 165–176.
- Lehman, D. E., Calderon, A. J., Moehle, J. P. (1995). Behavior and design of slender columns subjected to lateral loading. In *Proceedings of the 6th U.S. National conference on earthquake engineering*. Seattle, Washington, US.
- Li, H., Zhao, C., & Zhu, J. (2008). Research on structural design of power plants based on internal equipment. *Engineering Journal of Wuhan University*, 41(sup), 313–317.
- Li, J., & Ren, X. (2009). Stochastic damage model for concrete based on energy equivalent strain[J]. *International Journal of Solids and Structures*, 46(11–12), 2407–2419.
- Mander, J. B., Priestley, M. J. N., & Park, R. (1988). Theoretical stress-strain model for confined concrete. *Journal of Structural Engineering, ASCE*, 114(8), 1804–1826.
- Masukawa, J., Suda, K., & Maekawa, K. (1999). Three-dimensional nonlinear FEM analysis of hollow bridge piers considering spalling of concrete cover and buckling of reinforcing bars. *Transactions of the Japan Concrete Institute*, 21, 255–262.
- Mazzoni, S., & McKenna, F. (2003). OpenSees Examples Primer, Berkeley, USA.
- Mazzoni, S., McKenna, F., & Fenves, G. L. (2003). *Open system for earthquake engineering simulation (OpenSees)*. Berkeley USA: University of California.
- Menegotto, M., & Pinto, P. E. (1973). *Method of analysis for cyclically loaded RC plane frames including changes in geometry and non-elastic behavior of elements under combined normal force and bending*. Lisbon: International Association for Bridge and Structural Engineering.
- Nilson, A. H. (1968). Nonlinear analysis of reinforced concrete by the finite element method. *ACI Journal*, 65, 757–766.
- Phan, V., Saiidi, M. S., Aderson, J., & Ghasemi, H. (2007). Near-fault ground motion effects on reinforced concrete bridge columns. *Journal of Structural Engineering*, 133(7), 982–989.
- Priestly, M. J. N., & Benzoni, G. (1996). Seismic performance of circular columns with low longitudinal reinforcement ratios. *ACI Struct J*, 93(4), 474–475.
- Priestly, M. J. N., Seible, F., & Calvi, G. M. (1996). *Seismic design and retrofit of bridges*. New York, US: John Wiley and Sons.
- Ren, X., Chen, J. S., & Li, J. (2010). Micro-cracks informed damage models for brittle solids[J]. *International Journal of Solids and Structures*, 48(10), 1560–1571.
- Scott, B. D., Park, R., & Priestley, M. J. N. (1982). Stress-strain behavior of concrete confined by overlapping hoops at low and high rates. *ACI*, 79(1), 13–27.

- Shao, Y., Aval, S., & Mirmiran, A. (2005). Fiber-element model for cyclic analysis of concrete-filled fiber reinforced polymer tubes. *Journal of Structural Engineering*, 13(2), 292–303.
- Shirmohammadi, F., & Esmaeily, A. (2015). Performance of reinforced concrete columns under bi-axial lateral force/displacement and axial load. *Engineering Structures*, 99, 63–77.
- Wang, P., Han, Q., & Du, X. (2014). Seismic performance of circular RC bridge columns with flexure-torsion interaction. *Soil Dynamics and Earthquake Engineering*, 66, 13–30.
- Xu, Y., Bai, G., & Zhu, J. (2015). Pseudo-dynamic test and numerical simulation of a large direct air-cooling structure. *The Structural Design of Tall and Special Buildings*, 24(4), 280–299.
- Zendaoui, A., Kadid, A., & Yahiaoui, D. (2016). Comparison of different numerical models of RC elements for predicting the seismic performance of structures. *International Journal of Concrete Structures & Materials*, 10(4), 461–478.